Inkinen, Sampo; Yao, Lide; van Dijken, Sebastiaan

Reversible thermal strain control of oxygen vacancy ordering in an epitaxial La0.5Sr0.5CoO3-delta film

Published in:
Physical Review Materials

DOI:
10.1103/PhysRevMaterials.4.046002

Published: 28/04/2020

Document Version
Publisher's PDF, also known as Version of record

Editors' Suggestion

Reversible thermal strain control of oxygen vacancy ordering in an epitaxial $La_{0.5}Sr_{0.5}CoO_{3-\delta}$ film

Sampo Inkinen, Lide Yao,* and Sebastiaan van Dijken†
NanoSpin, Department of Applied Physics, Aalto University School of Science, P.O. Box 15100, FI-00076 Aalto, Finland

(Received 22 November 2019; revised manuscript received 27 January 2020; accepted 9 March 2020; published 28 April 2020)

Reversible topotactic transitions between oxygen-vacancy-ordered structures in transition-metal oxides provide a promising strategy for active manipulation of material properties. While transformations between various oxygen-deficient phases have been attained in bulk $ABO_{3-\delta}$ perovskites, substrate clamping restricts the formation of distinct ordering patterns in epitaxial films. Using *in situ* scanning transmission electron microscopy (STEM), we image a thermally driven reversible transition in $La_{0.5}Sr_{0.5}CoO_{3-\delta}$ films on $SrTiO_3$ from a multidomain brownmillerite (BM) structure to a uniform new phase wherein oxygen vacancies order in every third CoO_x plane. Because temperature cycling is performed over a limited temperature range (25−385 °C), the oxygen deficiency parameter δ does not vary measurably. Under constant δ, the topotactic transition proceeds via local reordering of oxygen vacancies driven by thermal strain. Atomic-resolution imaging reveals a two-step process whereby alternating vertically and horizontally oriented BM domains first scale in size to accommodate the strain induced by different thermal expansions of $La_{0.5}Sr_{0.5}CoO_{3-\delta}$ and $SrTiO_3$, before the new phase nucleates and quickly grows above 360 °C. Upon cooling, the film transforms back to the mixed BM phase. As the structural transition is fully reversible and δ does not change upon temperature cycling, we rule out electron-beam irradiation during STEM as the driving mechanism. Instead, our findings demonstrate that thermal strain can solely drive topotactic phase transitions in perovskite oxide films, presenting opportunities for switchable ionic devices.

DOI: 10.1103/PhysRevMaterials.4.046002

I. INTRODUCTION

Active control over the concentration or distribution of oxygen vacancies in transition-metal oxides enables manipulation of their structural, magnetic, electronic transport, and optical properties via valence changes of the transition-metal ions and the altering of bond lengths and angles [1–5]. In perovskite oxides, oxygen vacancies may order into distinct patterns depending on the oxygen off-stoichiometry, thereby forming a homologous series of oxygen-deficient $ABO_{(3n-1)/n}$ structures. Many members of the homologous series are accessible in bulk perovskites by topotactic oxidation or reduction reactions [6–12]. For instance, $SrCoO_{(3n-1)/n}$ with $n = 2$, 3, 4, 5, 6, 7, and 8 has been realized [9–12]. Among the oxygen-deficient perovskite phases, $ABO_{2.5}$ ($n = 2$) has been investigated most. In this phase, oxygen vacancies occupy every second BO_x plane. The resultant stacking of BO_6 octahedra and BO_4 tetrahedra is known as the brownmillerite (BM) structure. BMs exhibit mixed electronic and ionic conductivity and are relevant for gas sensors, oxygen storage devices, oxygen membranes, and cathodes in solid oxide fuel cells [3,13–15].

In contrast to bulk samples, epitaxial films of perovskite oxides do not display the same plurality of oxygen-deficient $ABO_{(3n-1)/n}$ phases. Instead, $ABO_{3-\delta}$ films tend to favor one oxygen vacancy ordered structure, often the BM, and the perovskite phase over extended δ ranges. Epitaxial $SrCoO_{3-\delta}$ films are a good example. In this system, the $SrCoO_{2.5}$ BM phase ($n = 2$) transforms directly into the $SrCoO_3$ perovskite structure ($n = \infty$) during annealing in oxygen atmosphere at $\delta \approx 0.25$, without accessing any of the intermediate phases of the $SrCoO_{(3n-1)/n}$ homologous series [3,15,16]. Annealing in vacuum produces the reverse structural transition [3,16]. Direct phase boundaries or transformations between BM and perovskite structures are also reported for other epitaxial films, including $La_{1-x}Sr_xMnO_{3-\delta}$ [5,17,18], $SrFeO_{3-\delta}$ [19–21], and $La_{1-x}Sr_xCoO_{3-\delta}$ [22,23]. Other members of the $ABO_{(3n-1)/n}$ homologous series have been observed in some specific perovskite films. For instance, superstructures comprising a stacking of two or three CoO_6 octahedral layers and one CoO_4 tetrahedral layer, corresponding to $n = 3$ and 4, have been imaged in epitaxial $LaCoO_{3-\delta}$ films [24–26]. While several vacancy ordered structures with $2 < n < \infty$ can thus appear in perovskite films, reports on transformations between distinct oxygen-deficient phases, let alone reversible transitions, are rare [5,27–29].

Strain imposed by the substrate can drastically affect the properties of epitaxial $ABO_{3-\delta}$ films. For instance, misfit strain tunes the oxygen deficiency (δ) of the BM and perovskite phases of $SrCoO_{3-\delta}$ through a reduction of the oxygen activation energy [16,30,31]. Strain can also determine the orientation of oxygen vacancy ordered superstructures, as illustrated by studies on $La_{0.5}Sr_{0.5}CoO_{3-\delta}$ (LSCO) [32–34]. When grown onto a $LaAlO_3$ (001) substrate with smaller lattice parameter, a lattice mismatch of $\varepsilon = +1.3\%$ compresses the LSCO film, leading to the formation of a BM structure with the oxygen-deficient CoO planes oriented parallel to the substrate surface [32–36]. Hereafter, we will refer to this phase as horizontal BM (h-BM). Growth of oxygen-deficient LSCO on $SrTiO_3$ (001) ($\varepsilon = -1.8\%$), in contrast, results in

*lide.yao@aalto.fi
†sebastiaan.van.dijken@aalto.fi

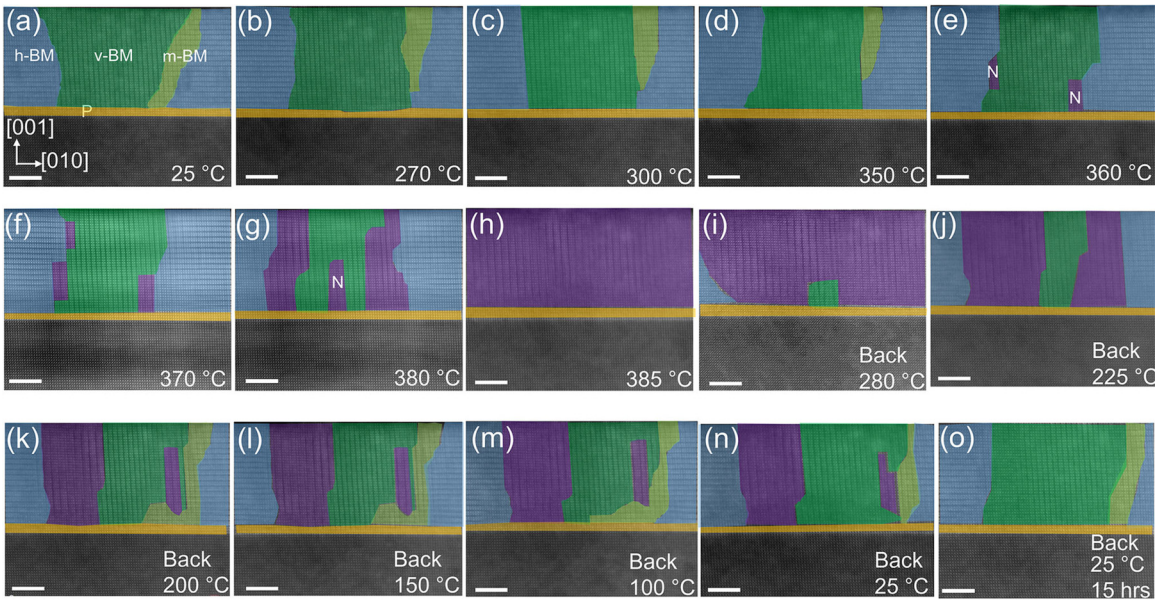

FIG. 1. Evolution of oxygen-vacancy-ordered domains during temperature cycling. (a–o) HAADF-STEM images of a 20-nm-thick epitaxial $La_{0.5}Sr_{0.5}CoO_{3-\delta}$ film on a $SrTiO_3$ substrate recorded during *in situ* heating and cooling. For clarity the structures are labeled and colored: perovskite (P, yellow), horizontal brownmillerite (h-BM, blue), vertical brownmillerite (v-BM, dark green), mixed h-BM and v-BM (m-BM, light green), and new phase (N, purple). The scale bars correspond to 5 nm.

a vertical BM (v-BM) structure [33,34,37] or a mixture of h-BM and v-BM domains [32,38]. Taking into account the larger average in-plane lattice parameter of v-BM compared to h-BM, elastic arguments do explain the growth of differently oriented BM phases as an instrument to relax misfit strain through oxygen vacancy ordering [33].

Because most experiments on topotactic phase transitions in $ABO_{3-\delta}$ films are performed by annealing in vacuum or oxygen atmosphere, the effects of strain are often masked by simultaneous changes in oxygen deficiency. Yet, strain can be a significant factor, as illustrated by strong changes in the reversibility of redox reactions in $SrCoO_{3-\delta}$ films grown onto different substrates [16]. To isolate the effects of strain on oxygen vacancy migration and ordering in perovskite films, one needs to perform experiments that allow for constant tuning of ε while δ is kept constant. Here, we use *in situ* scanning transmission electron microscopy (STEM) to demonstrate that thermal strain by itself can drive reversible topotactic transitions between distinct vacancy-ordered structures in an epitaxial $ABO_{3-\delta}$ film. Our results shed light on strain-structure relationships in oxygen-deficient perovskites and the atomic-scale dynamics of oxygen vacancy ordering, offering a promising mechanism for deterministic physical property control.

II. RESULTS AND DISCUSSION

Cross-sectional TEM specimens of a 20-nm-thick epitaxial LSCO film on a $SrTiO_3$ (STO) substrate were prepared for high-angle annular dark-field STEM (HAADF-STEM) analysis during *in situ* heating using a DENSsolutions Lightning D9+ holder (see the Appendix for details). In the as-grown state, the LSCO film exhibits alternating h-BM and v-BM structural domains, as illustrated by the orientation of atomic columns with bright and dark contrast in the HAADF-STEM images and clear superstructure reflections along the x and y axis of their fast Fourier transform (FFT) [see Fig. 1(a) and Fig. S1 of the Supplemental Material [39]]. The two BM structures exhibit a stacking sequence $La_{0.5}Sr_{0.5}O$-CoO_2-$La_{0.5}Sr_{0.5}O$-CoO_x along the [001] and [010] directions, respectively. Oxygen deficiency in the CoO_x layer enlarges the distance between the neighboring $La_{0.5}Sr_{0.5}O$ planes (dark contrast) and it reduces the spacing of $La_{0.5}Sr_{0.5}O$ planes separated by stoichiometric CoO_2 (bright contrast). Using the method by Kim *et al.* [40], which maps the oxygen vacancy concentration based on the local lattice parameter of the BM phase (Fig. S2 of the Supplemental Material [39]), we estimate $x = 1.25 \pm 0.06$. This composition corresponds to $La_{0.5}Sr_{0.5}CoO_{2.63\pm0.06}$ and, thus, $\delta = 0.37 \pm 0.06$. This oxygen deficiency matches $n \approx 2.7$ in the $La_{0.5}Sr_{0.5}CoO_{(3n-1)/n}$ homologous series, making transitions between structures corresponding to $n = 2$ and 3 possible. Because the oxygen vacancy concentration is lower than in the ideal BM structure ($\delta = 0.50$), the oxygen-deficient CoO_x layer comprises some CoO_6 octahedra or CoO_5 pentahedra in addition to the CoO_4 tetrahedra. Besides the h-BM and v-BM domains, the as grown LSCO film contains a few atomic layers with a perovskite structure near the STO substrate. Similar phase separation has been reported previously and was attributed to preferred oxygen vacancy formation near the film surface or disordering of oxygen vacancies under compressive strain near the film/substrate interface [34,41]. Small areas comprising a mixture of the two BM structures (m-BM) appear at some domain boundaries.

Next, we discuss the evolution of the LSCO film structure during *in situ* heating. In the experiments, we continuously increased the temperature of the TEM specimen at a rate of 8 °C/min while recording HAADF-STEM images. Figure 1

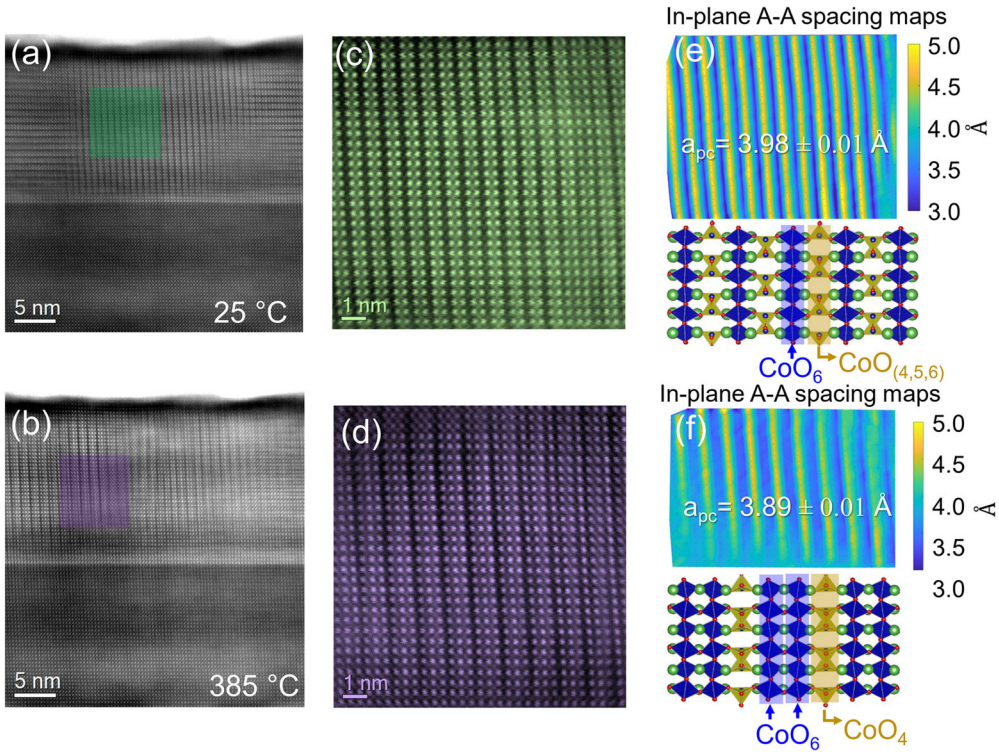

FIG. 2. (a–d) HAADF-STEM images and high-magnification closeups of a v-BM domain recorded at 25 °C (a, c) and an N domain recorded at 385 °C (b, d). Vertical lines with dark HAADF contrast indicate oxygen-deficient CoO_x planes with an expanded lattice parameter. (e, f) In-plane lattice spacing maps and structural models of (e) the v-BM phase and (f) the N phase.

summarizes a typical heating/cooling cycle. Here, we focus on a 30-nm-wide sample area. The selected area initially comprises two h-BM domains separated by a v-BM domain, which we colored blue and dark green for clarity (Figs. S3 and S4 of the Supplemental Material [39] show large uncolored versions of the same images and corresponding FFT patterns). Up to a temperature of 350 °C [Figs. 1(a)–1(d)], the h-BM domains grow slowly by lateral domain boundary motion at the expense of the v-BM domain. At 360 °C, a new structural phase (labeled N, purple color) nucleates at the h-BM/v-BM boundaries [Fig. 1(e)]. The appearance of extra reflections in the FFT besides the main reflections from the v-BM phase confirms the formation of a new vertically oriented superstructure (Fig. S3, Supplemental Material [39]). Up to 380 °C, the N phase gradually grows by replacing the original h-BM and v-BM domains and a new N domain nucleates in the center of the v-BM domain. After this, the N phase abruptly expands to the entire field of view at 385 °C, except for the perovskite structure (labeled P, yellow color) persisting near the STO substrate [Figs. 1(f)–1(h)]. The timescale of the structural transformation commencing at 360 °C and finalizing at 385 °C is 3 min. The transition from alternating h-BM/v-BM domains to the N phase is reversible, as illustrated by HAADF-STEM imaging during cool down [Figs. 1(i)–1(o)]. The h-BM and v-BM domains nucleate at the horizontal N/perovskite boundary and grow rapidly along the vertical direction. The subsequent lateral growth of these domains is slow and far from complete after reaching room temperature in about 45 min [see Fig. 1(n)]. Relaxation of the domains continues at 25 °C, as confirmed by the reestablishment of alternating h-BM and v-BM domains without the N phase after storing the sample in vacuum for 15 h [see Fig. 1(o)]. Local STEM–electron-energy-loss spectroscopy (EELS) measurements on the h-BM and v-BM domains and the N phase indicate that the heating/cooling cycle does not change the oxygen deficiency (δ) of the LSCO film (Fig. S5, Supplemental Material [39]). The reversible structural phase transition depicted in Fig. 1 thus demonstrates a significant reordering of existing oxygen vacancies as a function of temperature. Since oxygen vacancy migration is a thermally activated process, the transition from h-BM/v-BM domains to the N phase occurring at $T \geqslant 360$ °C is relatively fast, whereas the reverse route ensuing at lower temperatures takes more time.

We note that the fully reversible character of the experiments and the observation of constant δ rule out electron-beam irradiation as a possible driving mechanism. As previously demonstrated [18,22,28], electron-beam irradiation during (S)TEM characterization can trigger the formation and ordering of oxygen vacancies in perovskite films. This process, however, increases δ monotonically, thereby preventing a transition back into the original structural phase. To monitor the influence of the electron beam further, we tested the formation of the N phase far away from the STEM imaged area. There, we heated the sample to 385 °C without recording a series of images during heating. A fresh and quick measurement at the maximum temperature confirmed the formation of the N phase without any discernable structural differences.

Figure 2 compares high-resolution HAADF-STEM images of the v-BM phase at 25 °C and the N phase at 385 °C. In the v-BM structure, every second CoO_x plane is oxygen

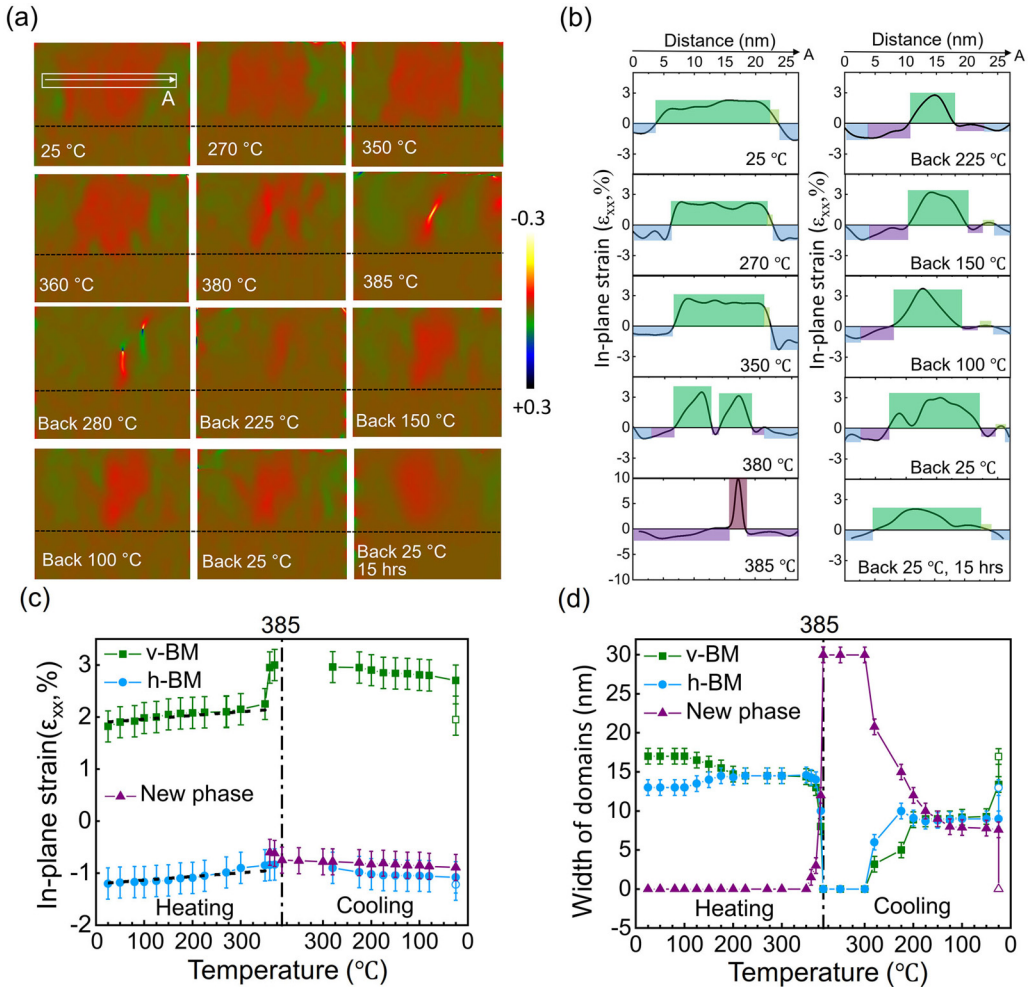

FIG. 3. (a) In-plane strain maps calculated from selected HAADF-STEM images in Fig. 1 (Fig. S6 of the Supplemental Material [39] shows a complete set of in-plane and out-of-plane strain maps). Dashed lines indicate the LSCO/STO interface. (b) In-plane strain profiles extracted from the maps in (a) along arrow A. The data are averaged over the area marked by a white box. Positive values of ε_{xx} represent a compressive in-plane strain along [010], whereas negative values of ε_{xx} indicate tensile strain. In (b) the same colors are used as in Fig. 1 to mark the structural domains. (c) Evolution of in-plane strain as a function of temperature in the different domains. The black dashed lines indicate calculations for h-BM and v-BM domains based on the difference in thermal expansions coefficients of the LSCO film and STO substrate. (d) Variation of the domain widths during heating and cooling.

deficient ($x < 2$) and the resulting lattice expansion produces stripes with dark HAADF contrast. The N structure exhibits a similar vertical stripe pattern, but now every third CoO_x plane exhibits dark contrast. The period of the oxygen-vacancy-ordered structure thus changes from $2a$ to $3a$ during the thermally induced phase transition. The appearance of superstructure reflections in the FTTs of Fig. S3 of the Supplemental Material [39] at $1/3a$ and $2/3a$ along the [010] direction and the concurrent disappearance of the $1/2a$ reflections during heating to 385 °C confirm the change of the modulation period. The N phase can be considered as the $n = 3$ member of the $La_{0.5}Sr_{0.5}CoO_{(3n-1)/n}$ homologous series. In fact, the ideal oxygen deficiency for this structure, $\delta = 0.33$, closely matches the value derived for our epitaxial LSCO film ($\delta = 0.37 \pm 0.06$). From this observation and the fact that δ remains constant during temperature cycling, we conclude that a new vertically oriented superstructure with CoO_4 tetrahedra in every third CoO_x plane replaces the v-BM and h-BM domains with a mixture of CoO_4 tetrahedra, CoO_5 pentahedra, and CoO_6 octahedra in every second CoO_x plane. Figures 2(e) and 2(f) show structural models for the v-BM and N phase together with in-plane lattice spacing maps corresponding to the STEM images of Figs. 2(c) and 2(d). The average pseudocubic lattice parameter along [010] measured far away from the LSCO/STO interface is $a_{pc} = 3.98 \pm 0.01$ Å for the v-BM structure and $a_{pc} = 3.89 \pm 0.01$ Å for the N phase.

Because the concentration of oxygen vacancies remains constant during the *in situ* STEM experiments, strain is the driving force behind the thermally induced structural phase transitions. In our nonstoichiometric LSCO film, the formation of alternating h-BM and v-BM domains reduces the elastic energy at room temperature [32,38]. The lattice mismatch between the h-BM phase ($a_{pc} = 3.86 \pm 0.01$ Å, measured far away from STO) and STO ($a = 3.905$ Å) is -1.2%, whereas the lattice mismatch between v-BM domains ($a_{pc} = 3.98 \pm 0.01$ Å on average along [010]) and STO is $+1.9\%$. Thus, based on elastic arguments [33], one would expect the more heavily strained v-BM domains to be smaller. Analyzing a

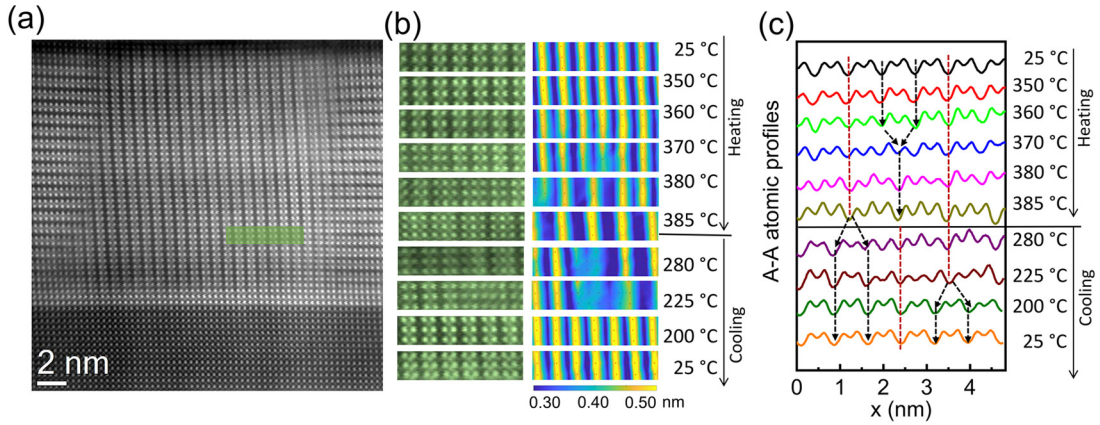

FIG. 4. Atomic-scale analysis of oxygen-vacancy migration dynamics during reversible transitions between the v-BM and N phases. (a) HAADF-STEM image of the initial LSCO film structure with the area under study marked in green. (b) Closeups of the green area recorded at different temperatures during heating and cooling. Corresponding in-plane lattice spacing maps are shown on the right. (c) HAADF-STEM intensity profiles extracted from the images in (b). Red dashed lines mark the oxygen-deficient CoO_x planes the locations of which remain fixed during heating/cooling. Black dashed lines and arrows indicate how two CoO_x planes combine into one (heating) or how one CoO_x plane splits into two (cooling).

large set of room-temperature STEM images, we find that this is indeed the case with the h-BM and v-BM domains having an average width of 45 and 20 nm, respectively. Upon heating the LSCO/STO sample, the strain state of the LSCO film changes because the linear thermal expansion coefficient of LSCO ($1.79 \times 10^{-5}\,^{\circ}C^{-1}$) [42] is larger than that of STO ($1.08 \times 10^{-5}\,^{\circ}C^{-1}$) [43]. Consequently, the compressive strain in the v-BM domains increases, while the tensile strain in the h-BM domains diminishes. Because of opposite changes in the elastic energy of the two domains, the h-BM phase grows slowly at the expense of the v-BM phase as the temperature increases, in agreement with the HAADF-STEM images of Figs. 1(a)–1(d). The in-plane strain maps and line profiles of Figs. 3(a) and 3(b), calculated by geometric phase analysis (GPA) of the images in Fig. 1, illustrate the evolution of lattice strain during temperature cycling. The compressive strain in the v-BM domain increases from +1.9% at room temperature to about +2.3% at 350 °C [Fig. 3(c)], which shrinks the domain gradually [Fig. 3(d)]. We note that the measured strain evolutions of the v-BM and h-BM domains in this temperature range agree with the calculated values of thermal strain [dashed black lines in Fig. 3(c)]. Further heating enhances the strain in the v-BM domain to an unsustainable level, triggering the nucleation of the N phase. The N phase nucleates at h-BM/v-BM boundaries and within the v-BM domain. The nucleation locations do demonstrate that relaxation of the thermally enhanced compressive strain in the v-BM domain indeed acts as the driving force behind the creation of N domains. Once formed, the N domains grow quickly at the expense of both the v-BM and h-BM phases until their replacement is complete at 385 °C [see Figs. 1(h) and 3(d)]. The disappearance of the h-BM domains at high temperature in favor of the N phase suggests that the latter is strained less on STO. While this conclusion is supported in part by the experimental data on in-plane strain along the [010] direction [−0.8% tensile strain in the N domain at 380 °C versus −1.0% strain in the h-BM domain at the same temperature, see Fig. 3(c)], the lattice mismatch along [100] (i.e., the direction of the electron beam in our *in situ* STEM experiments) should be considered in a full strain analysis. Finally, we note that the growth of the center and right N domains [see data for 380 °C in Fig. 3(b)] produces a stacking fault with an ill-defined GPA strain state upon domain coalescence at 385 °C. In the stacking fault, the period of the oxygen-vacancy-ordered structure is $2a$ instead of $3a$. Upon cooling, a v-BM domain nucleates and grows from the stacking fault at $T < 280\,^{\circ}C$ to relax the tensile strain of the N phase. Simultaneously, h-BM domains reform and the growth of both BM domains ultimately restores an alternating h-BM/v-BM domain pattern at room temperature. While energy minimization determines the average width of the h-BM and v-BM domains after cooling, the formation of stacking faults during temperature cycling affects their location. During subsequent temperature cycles, stacking faults can form at different locations. For a full GPA data set including out-of-plane strain maps see Fig. S6 of the Supplemental Material [39].

Figure 4 visualizes the atomic scale dynamics of oxygen vacancy reordering during reversible transitions between the v-BM and N structures. Here, we focus on a LSCO film area located in a v-BM domain at room temperature [marked green in Fig. 4(a)]. Upon heating the period of the oxygen-deficient CoO_x planes changes from $2a$ to $3a$ [Fig. 4(b)]. Figure 4(c) shows intensity profiles of HAADF-STEM images as a function of temperature to elucidate this process. Herein, deep intensity minima (dark contrast) correspond to oxygen-deficient CoO_x planes, shallow minima mark the location of stoichiometric CoO_2 planes, and intensity maxima depict $La_{0.5}Sr_{0.5}O$ planes. Starting at 25 °C, oxygen vacancies occupy every second CoO_x plane (v-BM phase). During the transition to the N structure at elevated temperatures, the position of every third oxygen-deficient CoO_x plane remains fixed [marked by dashed red lines in Fig. 4(c)]. Vacancies in the other oxygen-deficient CoO_x planes migrate to the oxygen stoichiometric CoO_2 plane that separates them initially [see black dashed lines and arrows in Fig. 4(c)]. As a result, the modulation period of the vertical oxygen-vacancy-ordered structure changes

from 2*a* to 3*a*. The oxygen-vacancy-driven transformations in the HAADF-STEM intensity profiles [Fig. 4(c)] and in-plane lattice spacing maps [Fig. 4(b)] are relatively fast, demonstrating completion of the v-BM to N phase transition in a narrow 360−385 °C temperature window. Upon cooling to room temperature, the reverse migration process ensues. Now, the position of every second oxygen-deficient CoO_x plane remains fixed [red dashed line in Fig. 4(c)], whereas the others split into two [black dashed lines and arrows in Fig. 4(c)]. Because the N to v-BM phase transition occurs at lower temperature, oxygen vacancy migration is less efficient. As a result, the transition takes more time and a larger degree of oxygen vacancy disorder develops during the structural transformation. The lattice spacing maps obtained at 280 and 225 °C [Fig. 4(b)] illustrate the latter point particularly well. In the selected LSCO film area of Fig. 4(a), the v-BM phase is fully reestablished at 200 °C. Interestingly, since the two CoO_x planes that combine into one during heating and the one CoO_x plane that splits into two during cooling are different in location, the v-BM superstructure undergoes a lateral shift by lattice parameter *a* during the full heating/cooling cycle. A similar analysis of oxygen vacancy reordering during the nucleation of the N phase at a h-BM/v-BM domain boundary is presented in Fig. S7 of the Supplemental Material [39]. Atomic-resolution HAADF-STEM images of the h-BM/v-BM boundary area reveal that the N phase nucleates on the v-BM side of the boundary, after which it quickly expands into both BM domains.

III. CONCLUSIONS

In summary, using *in situ* sample heating and STEM imaging, we demonstrate reversible topotactic transitions between two distinct oxygen-vacancy-ordered structures in an epitaxial $La_{0.5}Sr_{0.5}CoO_{3-\delta}$ film on $SrTiO_3$ (001). In contrast to studies where the oxygen deficiency parameter δ of a perovskite film is varied to induce a structural phase transition (oxidation/reduction reactions, electron-beam irradiation, electric-field control) [3–5,15–23,27–31], $\delta = 0.37 \pm 0.06$ is kept constant in our experiments. Under fixed oxygen off-stoichiometry, we find that thermal strain controls the occurrence of topotactic phase transitions. In our material system, a pattern of alternating h-BM domains (tensile strain) and v-BM domains (compressive strain) is energetically favorable at room temperature. The elastic energy of the LSCO film changes upon heating because its thermal expansion coefficient is larger than that of the STO substrate. Initially, this leads to the growth of h-BM domains at the expense of v-BM domains, but at 360 °C a new oxygen-vacancy-ordered structure emerges as the lowest-energy state under thermal strain. In the new phase, which covers the entire LSCO film at 385 °C, oxygen vacancies order into every third CoO_x plane rather than every second in the BM phase. Microscopically, a redistribution of oxygen vacancies whereby some CoO_x planes remain fixed and others combine into one explains the change of the modulation period from 2*a* to 3*a*. Upon cooling, the reverse topotactic phase transition ensues on a longer timescale because of reduced oxygen vacancy mobility at lower temperature.

Our results point to interesting perspectives. First, the presented *in situ* STEM experiments demonstrate a great sensitivity of oxygen-vacancy-ordered phases to small changes in lattice strain. Together with the strong dependence on the oxygen deficiency parameter, this opens up a playground for the engineering of distinct topotactic transitions in closed epitaxial systems with constant oxygen off-stoichiometry. Second, thermal strain control of oxygen vacancy ordering in perovskite transition-metal oxide films opens the door to reversible property manipulation, including magnetism, ferroelectricity, optical reflection/transmission, and electronic transport. Compared to crystalline-amorphous transitions in phase-change materials such as chalcogenide alloys that mainly alter their electrical resistivity [44,45], this broadens the application potential of thermally induced structural phase transitions.

ACKNOWLEDGMENTS

This work was supported by the Academy of Finland (Grants No. 293929, No. 304291, No. 319218, and No. 316857). TEM analysis was conducted at the Aalto University OtaNano–Nanomicroscopy Center.

APPENDIX: EXPERIMENTAL

1. Sample fabrication

A 20-nm-thick $La_{0.5}Sr_{0.5}CoO_{3-\delta}$ film was epitaxially grown on a single-crystal $SrTiO_3$ substrate using pulsed laser deposition (PLD). Before film growth, the substrate was etched in buffered hydrofluoric acid for 30 s and annealed in oxygen atmosphere at 950 °C for 1 h. This preparation process resulted in a TiO_2-terminated surface. We operated the PLD system using a 2.5-J cm^{-2} laser fluence and a 4-Hz pulse repetition rate. The $La_{0.5}Sr_{0.5}CoO_{3-\delta}$ film was deposited at 800 °C in an oxygen partial pressure of 0.2 mbar. After growth, we cooled the sample to room temperature in about 50 min using the same oxygen environment.

Cross-sectional STEM lamella were prepared by focused ion beam (FIB) milling using Ga^+ ions accelerated at 30 kV in a FEI Helios Nanolab 600 system. To reduce charging and ion-beam damage during FIB processing, we deposited a 30-nm-thick Pt/Ir conductive layer on top of the LSCO film using a sputtering system (Leica EM ACE600) before loading the sample into the FIB chamber. Next, a 1.5-μm-thick Pt structure with dimension $10 \times 2\,\mu$m was grown using ion-beam-induced deposition inside the FIB. After that, we defined a lamella by milling 6-μm-deep grooves next to the Pt-capped area. The lamella was lifted out of the sample using an OmniProbe manipulator and transferred onto a DENSsolutions heating nanochip. Finally, the cross-sectional lamella was fine polished to about 50 nm in thickness by Ar ion milling and the nanochip was mounted onto a DENSsolutions lightning D9+ holder for *in situ* STEM characterization.

2. *In situ* STEM experiments

HAADF-STEM imaging and local EELS analyses were carried out using a double Cs corrected JEOL 2200FS system operated at 200 kV. During the heating/cooling cycles, we

varied the sample temperature at a rate of 8 °C/min, which allowed us to image the real-time dynamics of the structural phase transitions and the underlying oxygen vacancy migration processes within the temperature range of the experiments. A heating coil on the DENSsolutions chip carrier was used to control the temperature of the sample. HAADF-STEM images were collected every 10 °C in the 25−200 °C temperature interval and every 5 °C above 200 °C. For each image, we used a pixel time of 16 µs. Thermal and epitaxial strains of the film were evaluated by geometric phase analysis of HAADF-STEM images using the FRWRtools plugin [46,47] implemented in DigitalMicrograph (Gatan, Inc.). For lattice analysis, the coordinates of the atomic columns were extracted using a two-dimensional Gaussian fitting script in Matlab and the lattice spacings were calculated by the Peak Pairs algorithm [48].

[1] S. V. Kalinin and N. A. Spaldin, Science **341**, 858 (2013).

[2] J. Jeong, N. Aetukuri, T. Graf, T. D. Schladt, M. G. Samant, and S. S. P. Parkin, Science **339**, 1402 (2013).

[3] H. Jeen, W. S. Choi, M. D. Biegalski, C. M. Folkman, I. C. Tung, D. D. Fong, J. W. Freeland, D. Shin, H. Ohta, M. F. Chisholm, and H. N. Lee, Nat. Mater. **12**, 1057 (2013).

[4] N. Lu, P. Zhang, Q. Zhang, R. Qiao, Q. He, H.-B. Li, Y. Wang, J. Guo, D. Zhang, Z. Duan, Z. Li, M. Wang, S. Yang, M. Yan, E. Arenholz, S. Zhou, W. Yang, L. Gu, C.-W. Nan, J. Wu, Y. Tokura, and P. Yu, Nature (London) **546**, 124 (2017).

[5] L. Yao, S. Inkinen, and S. van Dijken, Nat. Commun. **8**, 14544 (2017).

[6] M. J. Sayagués, M. Vallet-Regí, A. Caneiro, and J. M. González-Calbet, J. Solid State Chem. **110**, 295 (1994).

[7] O. H. Hansteen, H. Fjellvåg, and B. C. Hauback, J. Mater. Chem. **8**, 2081 (1998).

[8] J. P. Hodges, S. Short, J. D. Jorgensen, X. Xiong, B. Dabrowski, S. M. Mini, and C. W. Kimball, J. Solid State Chem. **151**, 190 (2000).

[9] A. Nemudry, P. Rudolf, and R. Schöllhorn, Chem. Mater. **8**, 2232 (1996).

[10] R. Le Toquin, W. Paulus, A. Cousson, C. Prestipino, and C. Lamberti, J. Am. Chem. Soc. **128**, 13161 (2006).

[11] L. Karvonen, H. Yamauchi, and M. Karppinen, Chem. Mater. **20**, 7143 (2008).

[12] L. Karvonen, S. Yoon, P. Hug, H. Yamauchi, A. Weidenkaff, and M. Karppinen, Mater. Res. Bull. **46**, 1340 (2011).

[13] J. B. Goodenough, Annu. Rev. Mater. Res. **33**, 91 (2003).

[14] S. B. Adler, Chem. Rev. **104**, 4791 (2004).

[15] H. Jeen, W. S. Choi, J. W. Freeland, H. Ohta, C. U. Jung, and H. N. Lee, Adv. Mater. **25**, 3651 (2013).

[16] S. Hu, Y. Wang, C. Cazorla, and J. Seidel, Chem. Mater. **29**, 708 (2017).

[17] J. D. Ferguson, Y. Kim, L. Fitting Kourkoutis, A. Vodnick, A. R. Woll, D. A. Muller, and J. D. Brock, Adv. Mater. **23**, 1226 (2011).

[18] L. Yao, S. Majumdar, L. Äkäslompolo, S. Inkinen, Q. H. Qin, and S. van Dijken, Adv. Mater. **26**, 2789 (2014).

[19] A. Khare, D. Shin, T. S. Yoo, M. Kim, T. D. Kang, J. Lee, R. Roh, I.-H. Jung, J. Hwang, S. W. Kim, T. W. Noh, H. Ohta, and W. S. Choi, Adv. Mater. **29**, 1606566 (2017).

[20] S. Roh, S. Lee, M. Lee, Y.-S. Seo, A. Khare, T. Yoo, S. Woo, W. S. Choi, J. Hwang, A. Glamazda, and K.-Y. Choi, Phys. Rev. B **97**, 075104 (2018).

[21] C. Ge, C.-X. Liu, Q.-L. Zhou, Q.-H. Zhang, J.-Y. Du, J.-K. Li, C. Wang, L. Gu, G.-Z. Yang, and K.-J. Jin, Adv. Mater. **31**, 1900379 (2019).

[22] J. H. Jang, Y.-M. Kim, Q. He, R. Mishra, L. Qiao, M. D. Biegalski, A. R. Lupini, S. T. Pantelides, S. J. Pennycook, S. V. Kalinin, and A. Y. Borisevich, ACS Nano **11**, 6942 (2017).

[23] D. A. Gilbert, A. J. Grutter, P. D. Murray, R. V. Chopdekar, A. M. Kane, A. L. Ionin, M. S. Lee, S. R. Spurgeon, B. J. Kirby, B. B. Maranville, A. T. N'Diaye, A. Mehta, E. Arenholz, K. Liu, Y. Takamura, and J. A. Borchers, Phys. Rev. Mater. **2**, 104402 (2018).

[24] W. S. Choi, J.-H. Kwon, H. Jeen, J. E. Hamann-Borrero, A. Radi, S. Macke, R. Sutarto, F. He, G. A. Sawatzky, V. Hinkov, M. Kim, and H. N. Lee, Nano Lett. **12**, 4966 (2012).

[25] N. Biškup, J. Salafranca, V. Mehta, M. P. Oxley, Y. Suzuki, S. J. Pennycook, S. T. Pantelides, and M. Varela, Phys. Rev. Lett. **112**, 087202 (2014).

[26] V. V. Mehta, N. Biškup, C. Jenkins, E. Arenholz, M. Varela, and Y. Suzuki, Phys. Rev. B **91**, 144418 (2015).

[27] Q. Zhang, X. He, J. Shi, N. Lu, H. Li, Q. Yu, Z. Zhang, L.-Q. Chen, B. Morris, Q. Xu, P. Yu, L. Gu, K. Jin, and C.-W. Nan, Nat. Commun. **8**, 104 (2017).

[28] Q. Q. Lan, X. J. Zhang, X. Shen, H. W. Yang, H. R. Zhang, X. X. Guan, W. Wang, Y. Yao, Y. G. Wang, Y. Peng, B. G. Liu, J. R. Sun, and R. C. Yu, Phys. Rev. Mater. **1**, 024403 (2017).

[29] L. Cao, O. Petracic, P. Zakalek, A. Weber, U. Rücker, J. Schubert, A. Koutsioubas, S. Mattauch, and T. Brückel, Adv. Mater. **31**, 1806183 (2019).

[30] J. R. Petrie, C. Mitra, H. Jeen, W. S. Choi, T. L. Meyer, F. A. Reboredo, J. W. Freeland, G. Eres, and H. N. Lee, Adv. Funct. Mater. **26**, 1564 (2016).

[31] J. R. Petrie, H. Jeen, S. C. Barron, T. L. Meyer, and H. N. Lee, J. Am. Chem. Soc. **138**, 7252 (2016).

[32] J. Gazquez, S. Bose, M. Sharma, M. A. Torija, S. J. Pennycook, C. Leighton, and M. Varela, APL Mater. **1**, 012105 (2013).

[33] D. O. Klenov, W. Donner, B. Foran, and S. Stemmer, Appl. Phys. Lett. **82**, 3427 (2003).

[34] X. Rui and R. F. Klie, Appl. Phys. Lett. **114**, 233101 (2019).

[35] J. Walter, S. Bose, M. Cabero, G. Yu, M. Greven, M. Varela, and C. Leighton, Phys. Rev. Mater. **2**, 111404 (2018).

[36] S. Stemmer, A. J. Jacobson, X. Chen, and A. Ignatiev, J. Appl. Phys. **90**, 3319 (2001).

[37] M. A. Torija, M. Sharma, J. Gazquez, M. Varela, C. He, J. Schmitt, J. A. Borchers, M. Laver, S. El-Khatib, and C. Leighton, Adv. Mater. **23**, 2711 (2011).

[38] M. A. Torija, M. Sharma, M. R. Fitzsimmons, M. Varela, and C. Leighton, J. Appl. Phys. **104**, 023901 (2008).

[39] See Supplemental Material at http://link.aps.org/supplemental/10.1103/PhysRevMaterials.4.046002 for an estimation of the oxygen deficiency parameter, raw uncolored HAADF-STEM

images and corresponding FFT patterns, STEM-EELS data, a full set of strain maps, and oxygen-vacancy migration dynamics at a h-BM/v-BM domain boundary.

[40] Y.-M. Kim, J. He, M. D. Biegalski, H. Ambaye, V. Lauter, H. M. Christen, S. T. Pantelides, S. J. Pennycook, S. V. Kalinin, and A. Y. Borisevich, Nat. Mater. **11**, 888 (2012).

[41] K. Hirai, R. Aso, Y. Ozaki, D. Kan, M. Haruta, N. Ichikawa, H. Kurata, and Y. Shimakawa, ACS Appl. Mater. Interfaces **9**, 30143 (2017).

[42] H. L. Lein, K. Wiik, and T. Grande, Solid State Ion. **177**, 1795 (2006).

[43] D. de Ligny and P. Richet, Phys. Rev. B **53**, 3013 (1996).

[44] M. Wuttig, Nat. Mater. **4**, 265 (2005).

[45] M. H. R. Lankhorst, B. W. S. M. M. Ketelaars, and R. A. M. Wolters, Nat. Mater. **4**, 347 (2005).

[46] M. J. Hÿtch, F. Snoeck, and R. Kilaas, Ultramicroscopy **74**, 131 (1998).

[47] C. T. Koch, FRWRtools plugin, https://www.physics.hu-berlin.de/en/sem/software/software_frwrtools.

[48] P. L. Galindo, S. Kret, A. M. Sanchez, J.-Y. Laval, A. Yáñez, J. Pizarro, E. Guerrero, T. Ben, and S. I. Molina, Ultramicroscopy **107**, 1186 (2007).